With the recent research interest in tumor tracking and the growth of imaging technologies in the treatment room, real-time tumor tracking could be a real possibility in the near future. In this study existing data of tumor tracks and external breathing signals are utilized. The respiratory gating protocol at our institution is described, and based on the imaging performed under that protocol we select the information that could have been collected about the tumor position. Then, using data of tumor tracks correlated with external breathing signals from real patient treatments, we investigate, with a computer simulation, the effect that image-guided adaptation of the gating window during treatment can have on the residual tumor motion.

2. Methods and materials

Lung cancer patients at the Radiation Oncology Department of the Nippon Telegraph and Telephone Corporation (NTT) Hospital in Sapporo, Japan, were treated with stereotactic body radiation therapy using the Mitsubishi real-time radiation therapy (RTRT) system. The RTRT system requires fiducials to be implanted in or near the tumor. Two to four gold ball bearings were used for these patients. Two x-ray tubes are mounted on the ceiling and are turned on during the entire treatment. The resulting images were analyzed in real time providing the 3D coordinates of the fiducials. In addition, an external respiratory gating system, AZ-733V, was utilized. The AZ-733V system developed by Anzai Medical Systems utilizes a laser displacement probe to construct a 1D breathing signal. The result is a large amount of data of external breathing signals correlated with the 3D position of a fiducial in close proximity to the primary tumor being treated. There were a total of eight patients from which several data sets were available from multiple days and beam angles. These 'Hokkaido Data' were used retrospectively to perform the current study.

Under the respiratory gating protocol at our institution, kV fluoroscopy is acquired as part of patient setup to position and verify the gating window. The gate remains fixed and *cine* EPID images are acquired during treatment to monitor the position of the tumor. Under the assumption that the total delivery time for each fraction takes about 2 min we selected data sets from the Hokkaido Data that were at least 2 min long. As a result, the data summarized in table 1 were used for this analysis. Following our clinical gating protocol the following assumptions are made for this simulation: (1) for the first 15 s the tumor position information was obtained from kV fluoroscopy (patient setup) and (2) for the rest of the fractions it was obtained by MV EPID imaging (patient treatment). Consequently, for the first 15 s the tumor position is available during the whole breathing cycle, the remainder of the time, the tumor position information is only available during beam on. We are only concerned with motion in the superior–inferior direction, since it is typically the most significant source of motion. The standard treatment to which the image-guided adaptive gating method is compared was based on our gating protocol in which the gating window is set at the beginning of each fraction and then remains static throughout the delivery. Therefore, two different gating techniques were investigated: (1) a *fixed* gating window, during which the gating window is the same as the one obtained during setup and (2) an *adaptive* gating window, during which the gating window is changed intrafractionally based on the tumor position information obtained during beam on. The adaptive gating window technique does not require adjustment of the beam aperture or patient position during treatment, as is the case in DMLC or moving table delivery, respectively.

As described previously, for the first 15 s the tumor position (internal signal) is available for the entire time, along with an external breathing signal as shown in figure 2. We assume that only 3 mm of residual motion, R, will be clinically allowed. The residual motion is

Table 1. A summary of the number of patients and the number of fractions used in this analysis.

Patient	Fractions
1	2
2	11
3	9
4	8
5	4
6	11
7	14
8	16

estimated from the tumor position, Z, and the median of the tumor position, Z_m, inside the gating window. Residual motion is defined as

$$R = |Z - Z_m| . \tag{1}$$

We also calculated the internal reference tumor position, REF_INT, and the external reference end-exhale position, REF_EXT, by taking the average of all the internal and external exhale positions, as illustrated in figure 2. A transformation factor (TF) is calculated as a ratio of amplitude external (AE) to amplitude internal (AI) in order to translate the external to internal amplitude and vise versa. AE corresponds to the width of the gating window and AI corresponds to the range of tumor motion. The upper limit (UL) of the gating window is set such that the residual motion is two thirds (i.e. 2 mm) of the allowed residual motion (i.e. 3 mm). The lower limit (LL) is set to a position that would result in one third (i.e. 1 mm) of the allowed residual motion (by using TF multiplied by 1 mm).

For the fixed gating window technique, the gating window set at patient setup remained the same for the entire fraction. For the image-guided adaptive gating window technique, each time the beam turns on, the tumor position is obtained and the following parameters are calculated and used to update the gating window:

- Range, RG = Maximum − Minimum (tumor position)
- Shift, SF = $|Z_m$ − REF_INT|
- Spread, SP = RG + SF
- Residual correction, C = |RG − 3 mm|.

Figure 3 is used to illustrate the process of adapting the gating window. Figure 3(a) shows an example of a breathing signal with an initial fixed gate. At the first instance when the breathing signal falls in the gate, tumor position information is obtained (figure 3(b)). The gating window is divided into in-gate high and in-gate low (divided by REF_EXT). A third possible position for the minimum exhale position is the out-gate low position, as shown in figure 3(a). In figure 3(b) the tumor position recorded during beam-on time is shown. Also shown is an example of how the parameters defined earlier are calculated. These parameters are used by the algorithm in combination with the end-exhale position in relation to the gating window to run the algorithm shown in figure 3(c). In the algorithm, the spread (SP) and residual correction (C) are used to update the upper and lower bounds of the gating window, in an effort to keep SP less than 3 mm.

The following parameters were recorded: the residual motion at the 95th percentile (R95), the duty cycle (DC), the percentage of the beam-on time that results in residual motion that is greater than 3 mm (RG3) and the maximum residual motion (MXR). A paired one-sided t-test

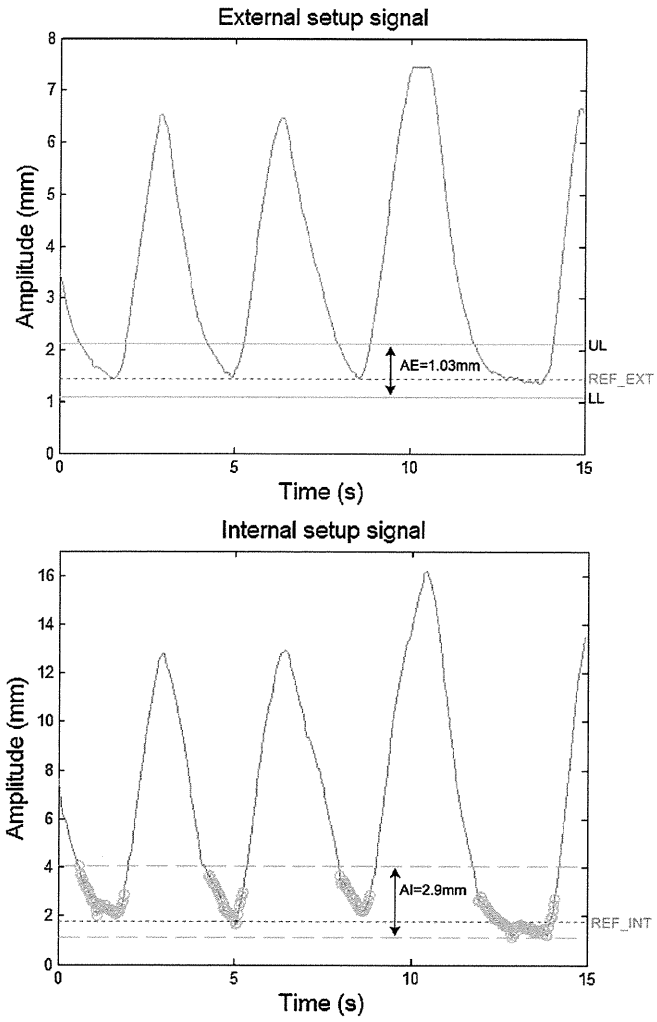

Figure 2. A sample external (top) and internal (bottom) setup signal. On the external signal plot the upper (UL) and lower (LL) limits of the gating window, the reference external position and the amplitude of the gate (AE) are indicated. On the internal signal plot the beam-on time (circles), internal reference position, and range of residual motion (AI) are indicated.

was performed to determine whether there was a statistically significant reduction in residual motion between the adaptive and fixed gating techniques. The image-guided adaptive gating window technique was run first, since it tends to result in lower beam-on time. The fixed gating window technique was then run with the same beam-on time in order to ensure that the same simulated 'number of MUs' was delivered.

3. Results

The tracking of the exhale position with the adaptive gating window technique is illustrated by the four cases shown in figure 4. The gating window was automatically adjusted to follow the

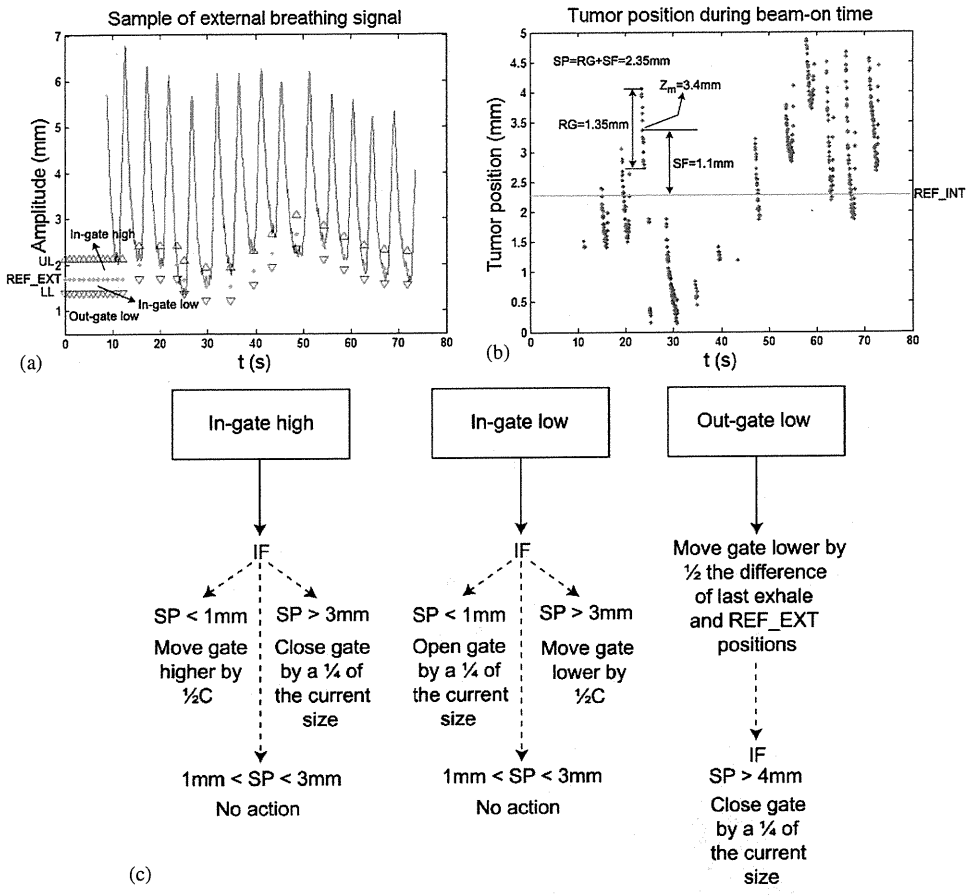

Figure 3. (a) An example external respiratory signal with the adapted gating window is shown. The triangles indicate the upper (UL) and lower (LL) limits of the gating window and the dots REF_EXT. (b) The corresponding internal signal is shown with the dots indicating the tumor position during the time the external signal falls in the gate. The measurement of some of the parameters used in updating the gate is illustrated. (c) The algorithm used to update the gate after each beam-on time.

exhale position when the respiratory signal drifted downward (figure 4(a)) and closed to allow for less residual motion in cases where the residual motion was larger than 3 mm (figure 4(b)). Furthermore, the exhale position was tracked even when the breathing signal was irregular (figure 4(c)) and the gate was opened to allow for more residual motion and increase the DC if the residual motion was smaller than 3 mm (figure 4(d)). The histograms of figure 4 illustrate that for all the cases shown the residual motion was reduced with the adaptive gating technique.

Table 2 summarizes the results of the two gating techniques for all eight patients. The difference in R95 between the fixed and adaptive gating techniques is statistically significant for five out of eight patients. The DC is higher for seven out of eight cases for the fixed gating technique, with the average being around 34%, while for the adaptive gating technique the average was 27%. Finally, RG3 and MXR were both smaller for the adaptive gating

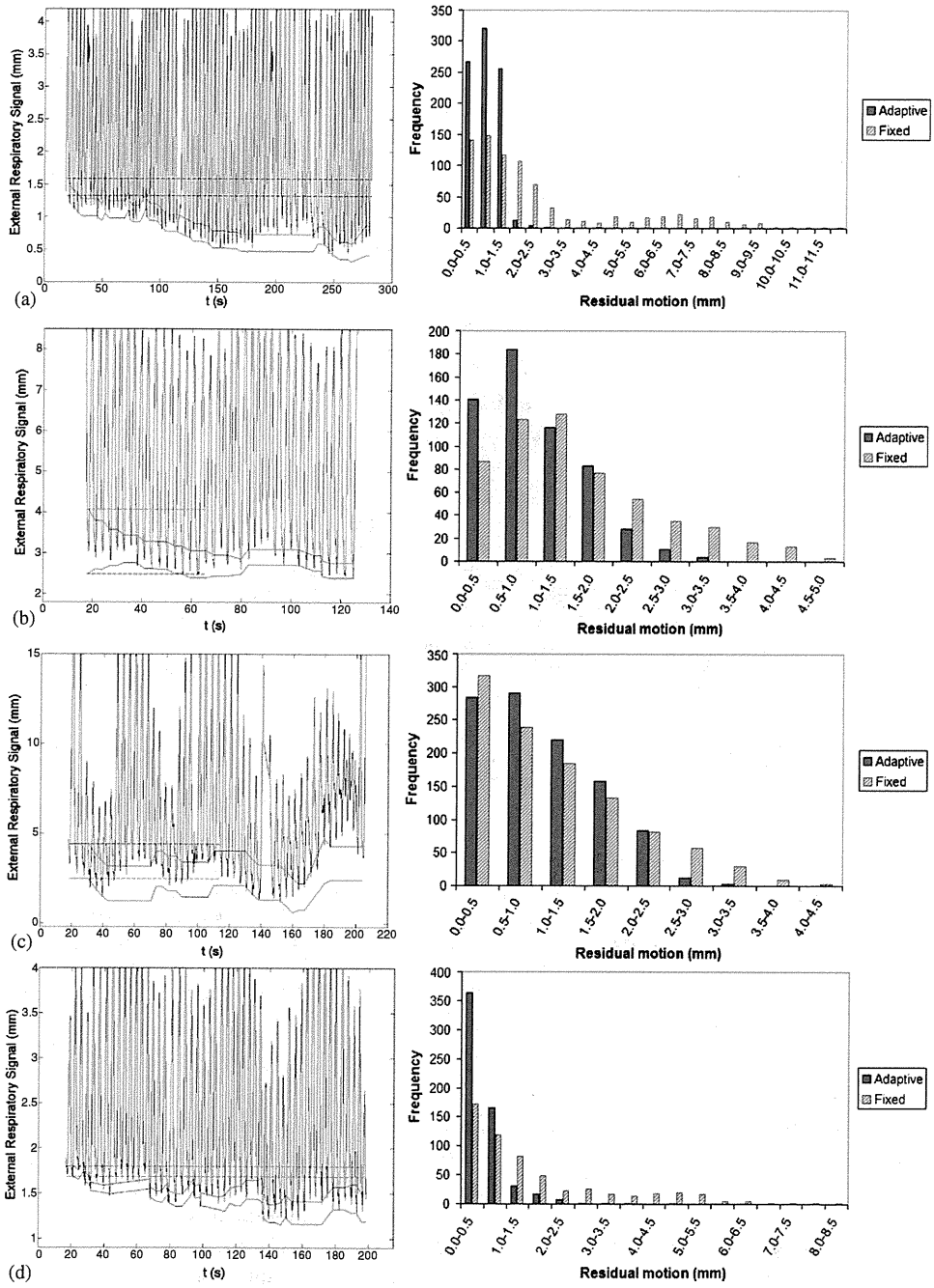

Figure 4. Four different treatment fractions showing the external signal (left) with the fixed (dotted line) and adaptive (continuous line) gating windows. The length of the fixed gating window signifies the duration of beam-on time. The residual tumor motion for the respective gating windows (right) is also shown.

Table 2. A summary of all the measurements made for the fixed and adaptive gating window techniques.

	R95 (mm)		DC (%)		RG3 (%)		MXR (mm)	
Patient	Fixed	Adaptive	Fixed	Adaptive	Fixed	Adaptive	Fixed	Adaptive
1†	2.1 ± 0.1	1.9 ± 0.1	57 ± 7	54 ± 7	0.3 ± 0.4	0.03 ± 0.04	3.4	3.1
2†	2.3 ± 0.7	1.9 ± 0.3	43 ± 8	33 ± 11	2.1 ± 3.2	0.3 ± 0.3	4.4	3.9
3	2.2 ± 0.5	2.6 ± 0.4	31 ± 28	19 ± 6	0.3 ± 0.4	0.9 ± 0.9	3.2	3.7
4	2.6 ± 0.8	2.2 ± 0.8	42 ± 13	34 ± 13	4.3 ± 6.1	2.1 ± 4.2	5.1	4.7
5	2.9 ± 1.1	4.7 ± 2.9	17 ± 11	9 ± 3	7.2 ± 12.6	13.5 ± 15.2	4.9	20.3
6†	3.0 ± 0.8	2.5 ± 0.6	33 ± 12	19 ± 4	6.8 ± 6.9	2.2 ± 4	5.6	4.3
7†	2.0 ± 0.4	1.8 ± 0.3	36 ± 7	29 ± 8	0.5 ± 0.7	0.3 ± 0.9	4.2	4.2
8†	2.9 ± 1.7	1.8 ± 0.7	12 ± 8	15 ± 9	6.5 ± 7.6	1.5 ± 3.1	11.6	6.8
Average	2.5	2.4	33.8	26.5	3.5	2.6	5.3	6.4

† Indicates statistically significant difference in R95 between the fixed and adaptive gating techniques. The p-values for patients 1, 2, 6, 7 and 8 are 0.012, 0.003, 0.002, 0.010 and 0.011, respectively.

technique for six out of eight patients. It was interesting to note that the data from two patients (3 and 5) were the ones that consistently showed a worse performance with the adaptive gating technique. We observed that some of the fractions (particularly for patients 3 and 5) used for this analysis had highly irregular breathing patterns, as the one shown in figure 4(c). Since the adaptive gating technique was designed specifically to track smooth changes in the breathing pattern (such as the baseline drifts shown in figures 4(a) and (d)) it did not perform well with some of the abrupt changes in the highly irregular breathing patterns.

After a closer examination of all the breathing patterns, we went through the analysis again by leaving out certain cases of highly irregular breathing patterns, under the assumption that patients under breath coaching would breathe relatively normally (Neicu *et al* 2006, Kini *et al* 2003). This resulted in leaving out patients 3 and 5 as well as fractions 8 (figure 4(c)), 1 and 6 from patients 2, 4 and 7, respectively, and fractions 2, 3, 4, 6, 7 and 14 from patient 8. The remaining data reflected more stable or smoothly varying breathing patterns. Figure 5 summarizes the results of the remaining patients, after leaving out the fractions with highly irregular breathing cycles.

Figure 5 shows that for all six patients R95 was reduced with the difference being statistically significant in all six cases (p-value < 0.025). On average, R95 was reduced by 24% with the adaptive gating window technique, going from 2.5 mm with the fixed gating window technique to 1.9 mm. The average R95 was larger than 3 mm for two patients (6 and 8*) for the fixed gating window, while for the adaptive gating window the largest average R95 was 2.5 mm. The DC was lower for all but one patient for the adaptive gating window with the average being 31% versus 38.5%. In total, the DC was greater than 20% for 42 out of 52 fractions for the fixed and 39 out of 52 fractions for the adaptive gating window techniques. The variations in the DC were quite large, with the fixed gating window ranging from 15% to 57%, while with the adaptive gating window ranging from 16% to 54%. The percentage of beam-on time that resulted in residual tumor motion greater than 3 mm was lower for all six cases for the adaptive gating technique. The maximum average value for the adaptive gating technique was only about 2% (patient 6) while reaching 8% (patient 8*) for the fixed gating window technique.

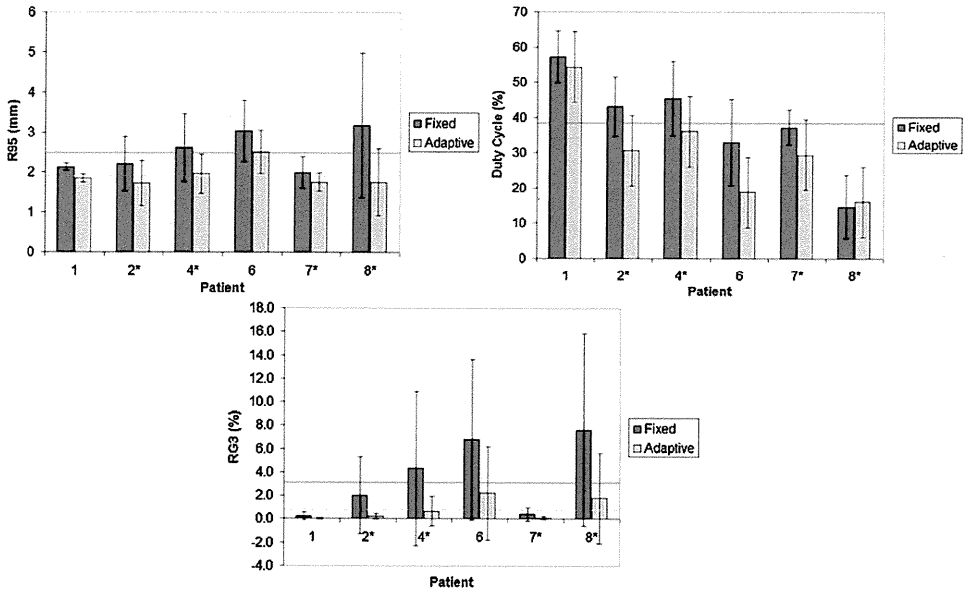

Figure 5. A plot of the residual motion (R95), DC and percent above 3% (RG3) for each patient and each gating technique (fixed and adaptive). The error bars on each plot reflect the standard deviation. The solid line indicates the mean of all fractions for the fixed gating technique and the dotted line the mean of all fractions for the adaptive gating technique. *Irregular breathing patterns excluded.

4. Discussion

Respiratory gating for radiation therapy as implemented in our clinic resembles the fixed gating window technique simulated in this study. If there is no information about the position of the tumor during treatment two main issues arise: baseline drifts and time shifts. There is no way of dealing with these issues without disruption of the treatment process. Baseline drifts could be identified by monitoring the breathing trace, but before the treatment is interrupted to re-adjust the gating window, several MUs could be delivered at the wrong phase of the breathing cycle. Furthermore, even if a baseline drift is identified on time, it can cause delays in the treatment, since the treatment has to be stopped and the internal/external signal correlation must be reassessed. In addition, the time shifts cannot be identified unless there is information about the position of the tumor during treatment. The lack of monitoring means uncertainty, which can result in large residual motion and consequently in marginal misses.

Several studies have investigated updating of the internal/external correlation during treatment (Schweikard *et al* 2000, Kanoulas *et al* 2007, Wu *et al* 2008). Schweikard *et al* (2000), utilizing the CyberKnife system, update the internal/external correlation between a marker placed on the patient's abdomen and periodic x-ray images taken every 10 s. Kanoulas *et al* (2007) investigated the updating of the correlation based on a pair of radiographic images taken at a fixed frequency during treatment. Both methods result in an extra dose from kV and they do not necessarily monitor what would happen during beam-on time, in a gated treatment. Our approach is similar to the approach taken by Wu *et al* (2008) in that it is specifically designed for respiratory gating. In their study, the internal/external correlation updating happens from information obtained during the beam-on time; however, it is based on information obtained from a single image.

The method we propose utilizes beam's-eye-view images obtained during the entire beam-on time. In addition with our method the residual motion is directly measured and the gating window is adapted with the goal to keep the residual motion below a certain level and not just to correlate internal and external signals. The results illustrate that updating the gating window based on information obtained during the previous beam-on time may give enough information to successfully track the end-exhale position, and follow smooth baseline drifts. With our method the correlation of the internal and external signals is not directly updated during treatment. The issue of changing correlation is dealt with in an indirect manner by compensatory widening and narrowing of the gating window. There could be cases in which the time shift is so large that the residual motion cannot be kept below 3 mm, without having a significantly reduced DC. In such cases the efficacy of gating using external surrogates should be reassessed and alternate treatment methods might be more appropriate. In general, with the adaptive gating technique the DC was reduced; however it was still acceptable with an average of 27% for all eight patients.

Apart from the reduction in the DC, another disadvantage of the adaptive gating window technique is that it relies on tracking the tumor on MV and kV images. That tracking can also be associated with an uncertainty, which the fixed gating window technique does not have, and has to be included in planning. However, with the adaptive gating window technique the allowed residual tumor motion is chosen before the treatment (in this case it was 3 mm) and as the top left plot of figure 5 illustrates, R95 can be kept below that goal for all of the patients. The added level of reliability could result in a reduction of the safety margins.

There was a statistically significant reduction in the DC (p-value $= 0.012$) going from the fixed to the adaptive gating window technique. We investigated whether the reduction in the residual tumor motion was purely a consequence of the reduced DC. The residual tumor motion, R95, was calculated only for the cases where the adaptive gating technique resulted in an increase in the DC. A total of 22 fractions were included in that analysis. It was found that while there was a statistically significant increase (p-value < 0.001) in the DC (15 to 19% on average) there was also a decrease in the residual tumor motion (from 2.5 to 1.9 mm on average), with a borderline significant t-test result (p-value $= 0.046$). In addition, the correlation between the change in the DC and the change in the residual tumor motion between the fixed and adaptive gating window techniques was close to zero (0.09) for all the fractions. Combining these results points to the fact that the reduction in R95 was a product of tumor tracking during treatment. Moreover, even if some of the reduction in the R95 came from a reduction in the DC that would have been necessitated by the algorithm to keep the residual motion low, which is the ultimate goal.

The available data were taken from the patients breathing freely, which resulted in breathing patterns for some treatment fractions that had highly variable breathing periods, drifting and variable peak-to-peak amplitudes. By leaving out these highly irregular breathing patterns we showed that the residual tumor motion could be reduced for the adaptive gating technique (2.4 mm to 1.9 mm), but not for the fixed gating window (2.5 mm for both). This suggests that the image-guided adaptive gating technique needs to be combined with breath coaching in order to be more effective. It also suggests that breath coaching alone cannot help reduce residual motion. Residual tumor motion is significantly lower for the adaptive gating window technique for all patients with more regular breathing patterns. In addition, the percentage of time that the residual motion is above 3 mm is quite low for the adaptive gating window, with the maximum average value being only 2% for all the patients. This suggests not only that the residual tumor motion is reduced overall, but also that it is done in a more reliable manner, since it results in only a few instances having residual motion larger than 3 mm.

5. Conclusions

The computer simulation study presented with this work demonstrates how information obtained with the imaging (kV/MV) performed under our current clinical gating protocol could be utilized to track the exhale tumor position before and during treatment. The result is an adaptive gating window that leads to a decrease in the residual tumor motion, as demonstrated using real patient data. This is based on the assumption that fast and reliable algorithms can be employed for direct tumor tracking on both MV and kV images. The evolution of research in this field suggests that the clinical realization of this may not be far in the future. With kV/MV imaging and real-time image processing, image-guided adaptive gating can result in consistent reduction of the residual tumor motion, which in turn could facilitate the reduction of margins used to account for tumor motion.

References

Adamson J *et al* 2008 Prostate intrafraction motion evaluation using kV fluoroscopy during treatment delivery: a feasibility and accuracy study *Med. Phys.* **35** 1793–806

Arimura H *et al* 2009 Computerized method for estimation of the location of a lung tumor on EPID cine images without implanted markers in stereotactic body radiotherapy *Phys. Med. Biol.* **54** 665–77

Arriagada R *et al* 1991 ASTRO (American Society for Therapeutic Radiology and Oncology) plenary: effect of chemotherapy on locally advanced non-small cell lung carcinoma: a randomized study of 353 patients. GETCB (Groupe d'Etude et Traitement des Cancers Bronchiques), FNCLCC (Féderation Nationale des Centres de Lutte contre le Cancer) and the CEBI trialists *Int. J. Radiat. Oncol. Biol. Phys.* **20** 1183–90

Berbeco R I *et al* 2005 Residual motion of lung tumours in gated radiotherapy with external respiratory surrogates *Phys. Med. Biol.* **50** 3655–67

Berbeco R I *et al* 2007 Clinical feasibility of using an EPID in CINE mode for image-guided verification of stereotactic body radiotherapy *Int. J. Radiat. Oncol. Biol. Phys.* **69** 258–66

Berbeco 2009 Marker-less verification of respiratory-gated radiotherapy for lung cancer *Med. Phys.* **36** 2491

Chi P *et al* 2006 Relation of external surface to internal tumor motion studies with cine CT *Med. Phys.* **33** 3116–23

Cho B *et al* 2009 First demonstration of combined kV/MV image-guided real-time dynamic multileaf-collimator target tracking *Int. J. Radiat. Oncol. Biol. Phys.* **74** 859–67

Curran W J *et al* 2003 Long-term benefit is observed in a phase III comparison of sequential versus concurrent chemo-radiation for patients with unresected stage III NSCLC: RTOG 9410 *Proc. Am. Soc. Clin. Oncol.* **22** 2499 (abstract)

D'Souza W D *et al* 2005 Real-time intra-fraction-motion tracking using the treatment couch: a feasibility study *Phys. Med. Biol.* **50** 4021–33

Ford E C *et al* 2003 Respiration-correlated spiral CT: a method of measuring respiratory-induced anatomic motion for radiation treatment planning *Med. Phys.* **30** 88–97

Hugo G *et al* 2006 Changes in the respiratory pattern during radiotherapy for cancer in the lung *Radiother. Oncol.* **78** 326–31

Ionascu D *et al* 2007 Internal–external correlation investigations of respiratory induced motion of lung tumors *Med. Phys.* **34** 3893–903

Jemal A *et al* 2009 Cancer statistics *CA Cancer J. Clin.* **59** 225–49

Kanoulas E *et al* 2007 Derivation of the tumor position from external respiratory surrogates with periodical updating of the internal/external correlation *Phys. Med. Biol.* **52** 5443–56

Kini V R *et al* 2003 Patient training in respiratory-gated radiotherapy *Med. Dosim.* **28** 7–11

Kontrisova K *et al* 2006 Dosimetric comparison of stereotactic body radiotherapy in different respiration conditions: a modeling study *Radiother. Oncol.* **81** 97–104

Korreman S S *et al* 2008 Respiratory gated beam delivery cannot facilitate margin reduction, unless combined with respiratory correlated image guidance *Radiother. Oncol.* **86** 61–8

Lin T *et al* 2009 Markerless gating for lung cancer radiotherapy based on machine learning techniques *Phys. Med. Biol.* **54** 1555–63

Mao W *et al* 2008 A fiducial detection algorithm for real-time image guided IMRT based on simultaneous MV and kV imaging *Med. Phys.* **35** 3554–64

Meyer J *et al* 2006 Tracking moving objects with megavoltage portal imaging: a feasibility study *Med. Phys.* **33** 1275–80

Murray B *et al* 2007 Frame-based immobilization and targeting for stereotactic body radiation therapy *Med. Dosim.* 32 86–91

Neicu T *et al* 2006 Synchronized moving aperture radiation therapy (SMART): improvement of breathing pattern reproducibility using respiratory coaching *Phys. Med. Biol.* 51 617–36

Nishioka S *et al* 2008 Exhale fluctuation in respiratory-gated radiotherapy of the lung: a pitfall of respiratory gating shown in a synchronized internal/external marker recording study *Radiother. Oncol.* 86 69–76

Nottrup T J *et al* 2007 Intra- and interfraction breathing variations during curative radiotherapy for lung cancer *Radiother. Oncol.* 84 40–48

Papiez L *et al* 2005 Real-time DMLC IMRT delivery for mobile and deforming targets *Med. Phys.* 32 3037–48

Purdie T G *et al* 2007 Cone-beam computed tomography for on-line image guidance of lung stereotactic radiotherapy: localization, verification, and intrafraction tumor position *Int. J. Radiat. Oncol. Biol. Phys.* 68 243–52

Rottmann J *et al* 2009a Mutual information for beams-eye-view lung tumor tracking without radiopaque markers *Med. Phys.* 36 2431

Rottmann J *et al* 2009b Multi-region tracking for lung tumor motion assessment *Int. Conf. on Machine Learning and Applications* pp 489–93

Schweikard A *et al* 2000 Robotic motion compensation for respiratory movement during radiosurgery *Comput. Aided Surg.* 5 263–77

Sonke J *et al* 2005 An off-line 4D cone beam CT based correction protocol for lung tumor motion *Int. J. Radiat. Oncol. Biol. Phys.* 63 S389–90

Vedam S *et al* 2001 Determining parameters for respiration-gated radiotherapy *Med. Phys.* 28 2139–46

Wiersma R D *et al* 2008 Combined kV and MV imaging for real-time tracking of implanted fiducial markers *Med. Phys.* 35 1191–8

Wu *et al* 2008 Gating based on internal/external signals with dynamic correlation updates *Phys. Med. Biol.* 53 7137–50

Xu Q *et al* 2008 Lung tumor tracking in fluoroscopic video based on optical flow *Med. Phys.* 35 5351–9

IOP PUBLISHING PHYSICS IN MEDICINE AND BIOLOGY

Phys. Med. Biol. **55** (2010) 3325–3337 doi:10.1088/0031-9155/55/12/005

Site-specific volumetric analysis of lung tumour motion

Eric W Pepin[1], Huanmei Wu[2], George A Sandison[3], Mark Langer[4] and Hiroki Shirato[5]

[1] School of Health Sciences, Purdue University, West Lafayette, IN 47907, USA
[2] Purdue School of Engineering and Technology, IUPUI, Indianapolis, IN 46202, USA
[3] Department of Radiation Oncology, University of Washington, Seattle, WA 98195, USA
[4] Indiana University School of Medicine, Indianapolis, IN 46202, USA
[5] Hokkaido University School of Medicine, Sapporo, Japan

E-mail: epepin@purdue.edu

Received 2 February 2010, in final form 13 April 2010
Published 26 May 2010
Online at stacks.iop.org/PMB/55/3325

Abstract

The treatment of lung cancer with radiation therapy is hindered by respiratory motion. Real-time adjustments to compensate for this motion are hampered by mechanical system latencies and imaging-rate restrictions. To better understand tumour motion behaviour for adaptive image-guided radiation therapy of lung cancer, the volume of a tumour's motion space was investigated. Motion data were collected by tracking an implanted fiducial using fluoroscopy at 30 Hz during treatment sessions. A total of 637 treatment fractions from 31 tumours were used in this study. For each fraction, data points collected from three consecutive breathing cycles were used to identify instantaneous tumour location. A convex hull was created over these data points, defining the tumour motion envelope. The study sought a correlation between the tumour location in the lung and the convex hull's volume and shape. It was found that tumours located in the upper apex had smaller motion envelopes (<50 mm^3), whereas tumours located near the chest wall or diaphragm had larger envelopes (>70 mm^3). Tumours attached to fixed anatomical structures had small motion spaces. Three general shapes described the tumour motion envelopes: 50% of motion envelopes enclosed largely 1D oscillation, 38% enclosed an ellipsoid path, 6% enclosed an arced path and 6% were of hybrid shape. This location–space correlation suggests it may be useful in developing a predictive model, but more work needs to be done to verify it.

(Some figures in this article are in colour only in the electronic version)

1. Introduction

In the administration of radiation therapy for lung cancer tumours, accurate dose delivery is challenged by respiratory-induced intra-fractional tumour motion (Keall *et al* 2006); this is

of particular importance in hypofractionated stereotatic radiosurgery. In one study, 50% of tumours had motion of at least 5 mm and 11% had motion greater than 10 mm (Chang *et al* 2008). This motion reduces the accuracy of the treatment and increases the uncertainty in the delivered dose, particularly when the motion extent is 1 cm or more (Keall *et al* 2001, Bortfeld *et al* 2002, Jiang *et al* 2003).

Tumour motion can be tracked accurately in real time, using techniques such as monitoring the anterior abdominal surface (Haasbeek *et al* 2007) or implanted fiducials (Shirato *et al* 2000). Such monitoring enables advanced image-guided radiation treatment of moving tumours, including the gated treatment delivery (RPM, Varian Medical Systems, Palo Alto, CA) and tumour tracking (CyberKnife Synchrony, Accuray, Sunnyvale, CA) (Haasbeek *et al* 2007, Smith *et al* 2009, Putra *et al* 2008, Ruan *et al* 2006, Vedam *et al* 2004). All the advanced motion compensation methods require an adequate understanding of motion characteristics. For example, in beam tracking, the important parameters of the tumour trajectory must be quantified to be used in treatment planning. Furthermore, these quantities must be continually monitored during treatment to ensure proper treatment delivery. Even though the precise three-dimensional (3D) locations of a moving tumour can be available in real time, radiation treatment delivery adjustments are hindered by mechanical system latencies and imaging-rate restrictions. The characterization of intra-fractional tumour motion helps the design of appropriate treatment approaches and enables the development of a predictive tumour motion behaviour model facilitating real-time image-guided radiation therapy (IGRT) of patients with free breathing during treatment.

Previous studies have focused on breathing characteristics such as amplitude and tidal volume (Yang *et al* 2008, Low *et al* 2005, Hoisak *et al* 2006, Chol *et al* 2008, Ren *et al* 2007, McCall and Jeraj 2007, Putra *et al* 2008, Wu *et al* 2007) for their descriptions of breathing behaviour, while mathematical models have been constructed using autoregressive moving averages (Ren *et al* 2007, McCall and Jeraj 2007) and combinations of periodic and semi-periodic functions (Putra *et al* 2008). The prediction models in these studies have had limited dependences on parameters related to tumour location in the lung and have lacked an overall description of tumour motion. The total volume occupied during breathing phases was investigated as the internal gross tumour volume (IGTV) (Kang *et al* 2007) using four-dimensional computed tomography (4DCT). Handels *et al* also calculated motion volume in this manner (Handels *et al* 2007). These volumes, however, are dependent on tumour volume and may not indicate the extent of tumour motion. The present study differs in that the volumes derived are indicative of real tumour motion.

This study is to investigate the relationship of tumour location in the lungs and motion characteristic, focusing on the space encompassed by lung tumours during treatment. We investigated the correlation between the size and shape of the tumour motion space with the location and attachment status of the tumour. Identified correlations may provide additional parameters useful in the development of a robust predictive model for future tumour motion in real-time adaptive IGRT.

2. Method and materials

2.1. Materials

This study used the 3D motion of implanted gold fiducials in 31 lung tumours during 637 radiotherapy fractions (ranged from 6 to 44 fractions per tumour) tracked using real-time fluoroscopy at a rate of 30 Hz at Hokkaido University (Shirato *et al* 2000). For each fraction, the motion of the tumour during the first three consecutive breathing cycles was studied. A

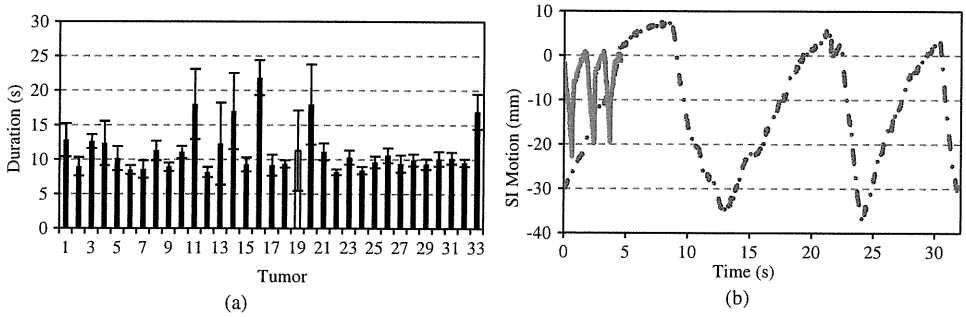

Figure 1. Data set durations. (a) For each tumor, the total duration of the three-breathing-cycle data set used in the analysis was averaged over all treatment fractions. Error bars show the standard deviation of all fractions. (b) The shortest three-breathing-cycle data set has 137 data points or 4.57 s (solid curve). The longest three-breathing-cycle data set has 964 data points or 32.1 s (dashed curve).

breathing cycle lasts about 3 to 5 s, and the average three-breathing-cycle data set size was 340 points. The cycle duration averaged over all treatment fractions for each patient is shown in figure 1(a).

The breathing cycle durations not only change from patient to patient but also from fraction to fraction, and even from one cycle to the next. The shortest and the longest three-breathing-cycle data sets are illustrated in figure 1(b). Incidentally, these are two different treatment sessions for the same tumor, as indicated by the white bar in (a). For one fraction, the breathing is fast and shallow, giving a total duration of 4.6 s for three cycles. For the other fractions, the breathing is slow and deep, giving a total duration of 32 s for three cycles. The figure also demonstrates intra-fractional inter-cyclic variations.

2.2. *Methods*

The motion envelope of the tumour in 3D space is calculated based on assigning a tumour position to a single point. This point was the position of one implanted fiducial in each tumour. Studies have shown the fiducial positions to be robust against migration (Kitamura *et al* 2002, Hashimoto *et al* 2005, Imura *et al* 2005, Shirato *et al* 2006, Katoh *et al* 2008, Onimaru *et al* 2005). The following three steps were used in the site-specific volumetric analysis of lung tumour motion.

(i) Outlier removal. Qualitatively, outliers can be defined as points that are physically separated from most other points and whose removal would substantially alter the size and/or shape of the motion envelope. Two criteria are proposed to identify outlier data points: one is based on motion velocity and the other is based on data point density. Motion velocity is limited by the patient's breathing frequency and amplitude. With an imaging rate of 30 Hz, fiducial displacement between frames is constrained by velocity. Furthermore, such a frequency makes it unlikely that the local neighbourhood of a fiducial position would not contain points collected in temporal proximity. Nakayama reported a maximum tumour velocity of 95.1 mm s^{-1} (Nakayama *et al* 2008).

Velocity-based outlier removal. The instantaneous velocity of the fiducial at each point was determined by dividing the absolute 3D Euclidean distance to it from the previous point by 1/30 s. Points were identified as outliers if their velocities were more than two standard

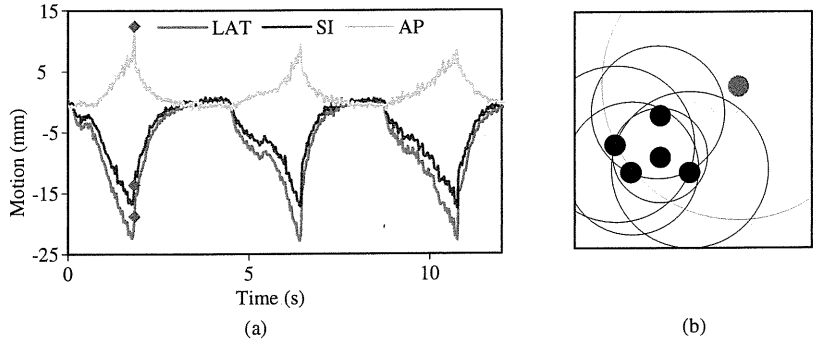

Figure 2. Outlier identifications. (a) An example of an outlier based on velocity: the instantaneous velocity of the tumour at 1.8 s (the three ♦ markers, one for each motion direction) is 4.54 standard deviations above the mean velocity in this treatment session. (b) A simplified example of an outlier based on density, where the circles enclose the nearest four points. The radius of the red/dashed circle is 1.9 standard deviations greater than the mean radius.

deviations above the mean velocity, where the mean and standard deviation are calculated by equations (1) and (2). Figure 2(a) shows a point near 2 s that is an outlier due to its high velocity:

$$\mu = \frac{1}{N-1}\sum_{i=2}^{N}\frac{\vec{r}_i - \vec{r}_{i-1}}{30\,s} \tag{1}$$

$$\sigma = \sqrt{\frac{\sum_{i=1}^{N}(v_i - \mu)^2}{N-1}}. \tag{2}$$

Density-based outlier removal. The second metric considered the 3D spatial density of the data points. For each data point, the ten closest data points were identified. The density of that data point was then described by the Euclidean distance from the point of interest to its tenth closest neighbour. A data point was identified as an outlier if its density measure was more than 1.8 standard deviations above the mean density measure of all data points in that fraction. In figure 2(b), the red data point is classified as an outlier due to its high density measure. These metrics corresponded well with a visual identification of outliers.

The exclusion of outliers is consistent with other prediction experiments (McCall and Jeraj 2007, Ren *et al* 2007).

(ii) Convex hull creation. After outlier removal, a convex hull was created about the remaining points and its volume calculated using the QHull algorithm implemented by the 'convhull' function in MatLab (Barber *et al* 1996). The volume of the convex hull for each treatment fraction was calculated. The tumour motion space was approximated as a convex hull because convex hulls are of minimally enclosing, well-defined shape that are computationally inexpensive and can relate the position of the fiducial marker at all times of the position sample set. The inter-fractional volumetric changes for each patient can be analysed by monitoring the convex hull volume change from one fraction to another.

In addition, the shapes of the convex hulls can be visually inspected. Several common convex hull shapes were discovered and mapped to the motion space of each fraction. This led to lung tumour motion classification based on the shapes of the motions space. For most

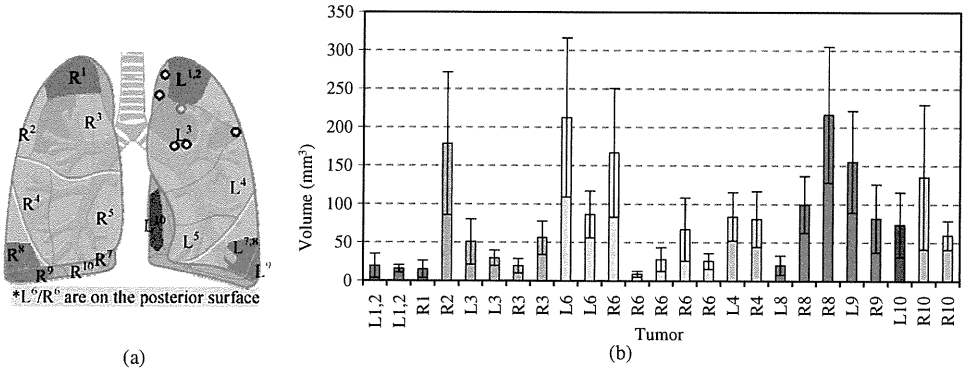

Figure 3. Site-specific volumetric change. (a) The shaded areas indicate the locations of free tumours, while circles indicate tumours that are attached to another structure (table 1). (b) Volumes of the convex hulls averaged over all the treatment fractions of free tumours (i.e. unattached). Error bars indicate the standard deviation.

of the fractions, a convex hull captured the motion space well. However, for some treatment fractions, motion patterns were better described as concave hulls, as discussed in detail below in section 4.

Kang *et al* (2007) described a similar concept, the IGTV, as the total volume occupied during breathing phases. Their study used 4DCT to discern tumour volumes. Handels *et al* (2007) also calculated motion volume in this manner.

(iii) Geometrical correlation analysis. In this work, each tumour's anatomic location was associated with the following four attributes: the pulmonary broncho-segment, the cranio-caudal location, the ventro-dorsal location and tumour adhesion to the cardiac wall. Combining these anatomic attributes along with tumour respiratory motion patterns enabled efficient tumour motion behaviour analysis and facilitated a better understanding of the anatomic effects on tumour motion.

Tumour locations were first categorized based on the bronchial segments (Sheffield 2009), as illustrated in figure 3(a). The upper apex lung region includes segments $L^{1,2}$ and R^1; the middle lung region includes segments L^3-L^5 and R^2-R^5; the peripheral lung region includes segments $L^{7,8}$-L^{10} and R^7-R^{10}; the whole posterior side of the lung is classified as segments L^6 and R^6. The volumetric changes and shapes of tumour motion were then mapped to the corresponding segments, as shown in figure 3(b). This mapping allowed a location–motion space comparison and determination of a correlation between volumetric variation and tumour location. For each tumour, the average volume of the motion space over all treatment sessions was related to tumour motion. The shape–location comparison was performed for individual treatment fractions. Additionally, the amplitude of motion during each fraction was calculated as the maximum Euclidian distance between two points of the fraction. This was compared to the volume of motion.

3. Results

3.1. Volume versus location results

Based on the geometrical mapping of tumours, the average tumour hull volume for each patient, averaged over all treatment fractions, is calculated and arranged in clusters according to the corresponding lung regions. Tumours located in the upper apex had smaller motion spaces

Table 1. Volume of each attached tumour motion envelope, along with its location and the anatomical structure to which it is attached, where the volume of the enclosing convex hulls is averaged over all treatment fractions of the patient. The uncertainty is the standard deviation. When compared to similarly located free tumours, p-values on the order of 10^{-5} are obtained.

Tumour location	Attached to	Motion space volume (mm^3)
$L^{1,2}$	Aorta	19.3 ± 8.2
$L^{1,2}$	Vertebra & aortic arch	71.0 ± 34.0
L^3	Posterior chest wall	25.7 ± 10.9
L^3	Lateral chest wall	6.5 ± 2.6
L^3	Aorta	58.7 ± 24.7
L^6	Anterior chest wall	30.4 ± 10.8

(median 15.7 mm^3; range 14.9–19.3 mm^3) as indicated by the red columns in figure 3(b). The middle region of the lung had slightly larger motion spaces (median 56.2 mm^3; range 19.5–178.8 mm^3), as indicated by the orange and green columns in figure 3(b). Peripheral tumours had the largest volumes (median 90.6 mm^3; range 20.6–216.6 mm^3), as indicated by the blue, purple and lavender columns in figure 3(b). There was considerable variation among posterior tumours, as indicated by the yellow columns in figure 3(b). For tumours attached to fixed anatomical structures, the motion space was small (these results are not shown in figure 3(b) but are summarized in table 1 instead). Considering location groups, p-values greater than 0.05 were found with t-tests comparing segments L3/R3 with L4/R4 (0.07) and L10 (0.53), L4/R4 with L10 (0.33), L8/R8/L9/R9 with R10 (0.50), and L10 with R10 (0.08). As L6/R6 covers the whole posterior, no t-tests were performed on the data from those segments.

3.2. Shape analysis

Three basic shapes and two hybrid shapes were observed to describe the spaces occupied by the respiratory motion paths of the fiducial markers during the three-cycle windows, as shown in figures 4 and 5. The shapes were inter-fractionally consistent, in general, but some tumours demonstrated a progressive change in the shape of their motion space as the number of treatment fractions advanced, as shown in figure 6.

For roughly half of the treatment fractions (49.8%), the tumours had rod-like motion spaces. Tumours moving accordingly have dominant motion amplitude in one dimension and relatively small ones in the other two dimensions. Figures 4(a) and (b) show an example of rod-like tumour motion. Note in this case that the 3D motion is symmetrical between the inhale state and exhale state over time.

Also prevalent were disc-shaped motion spaces, an example of which is shown in figures 4(c) and (d). When the tumour motion has a phase shift among different directions, especially between the two dominant directions, the motion creates an ellipse with a vacant centre presenting a disc-shaped hull. This shape of hull was seen for tumour motion in 38.3% of treatment fractions.

Lastly, in a small proportion of treatment fractions (6.0%), tumour motion followed an arc trajectory within the enclosing convex hull, as shown in figures 4(e) and (f). The convex hulls presented by this type of tumour motion contain much vacant space, resulting in an increased hull volume occupation. These types of motion spaces may be better described as concave

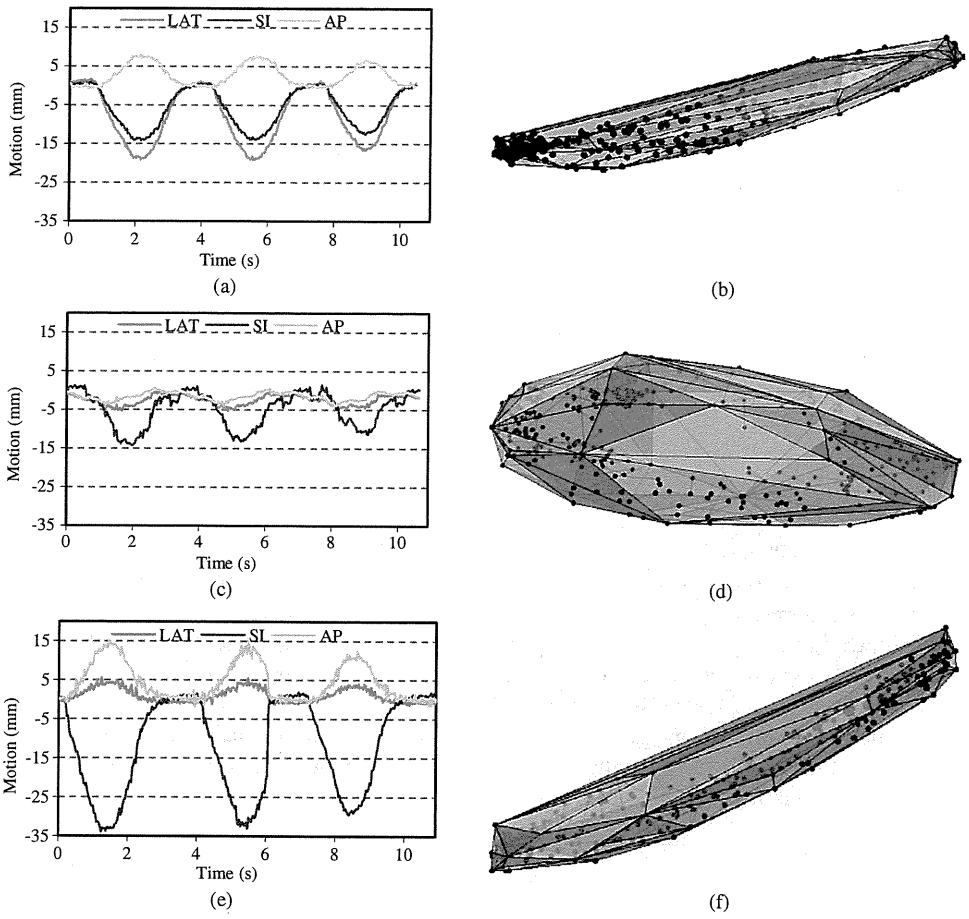

Figure 4. The motion characteristics and the hull shapes, where (a) and (b) are for rod-like hulls, (c) and (d) for disc-shaped hulls and (e) and (f) for arc-shaped hulls.

shapes. The motion versus time plots for tumours in these fractions have thicker tails at the end of exhalation.

Several treatment fractions had convex hulls that could best be described as hybrids of the three basic shapes. One of the more common hybrid shapes apparent in 4.4% of treatment fractions presented as a combination of the disc-shaped and arc-shaped hulls. Observation of the 3D tumour motion over time revealed that there was a phase shift during the late exhalation and a prolonged inhalation peak. This hybrid hull shape encompasses a considerable volume devoid of tumour location points, and so may be better described by a concave enclosure. An example of this hull shape is shown in figures 5(a) and (b).

Another hybrid hull shape for tumour motion that was observed in 1.6% of treatment fractions presented as a combination of rod-like and disc-shaped convex hulls. Also, these tumour motion paths were devoid of tumour location points near the hull centre but were distinguished from the elliptical paths of the disc-shaped hulls by their lack of path curvature. The 3D motion over time may be described as a tent function with sharp inhalation peaks, as shown in figures 5(c) and (d).

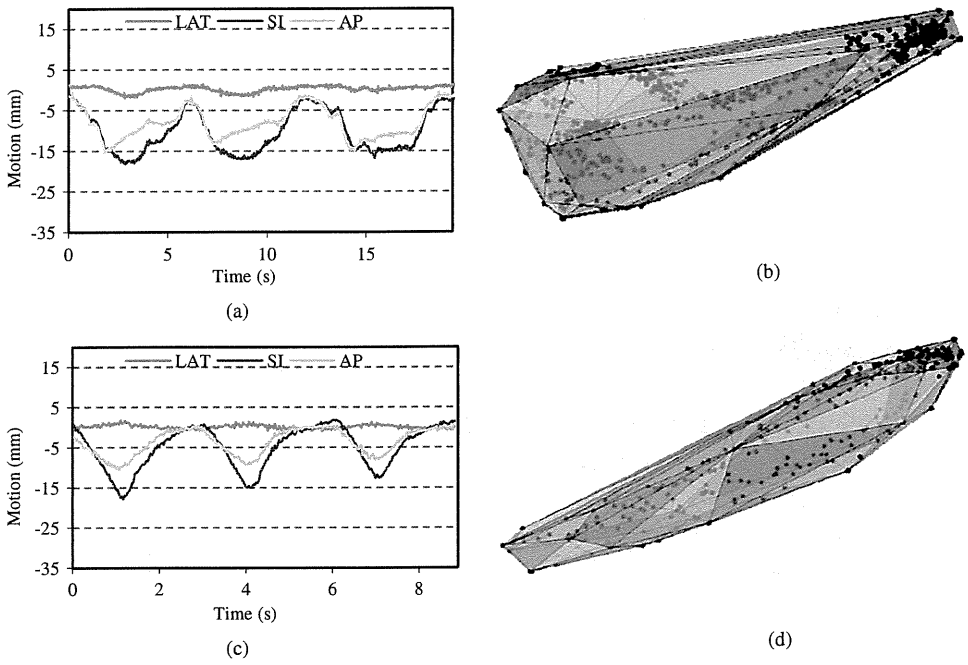

Figure 5. Tumour motion characteristics and hybrid hull shapes. A disc-shaped/arc-shaped hull example is shown in (a) and (b), while a rod-like-disc-shaped hull example is shown in (c) and (d).

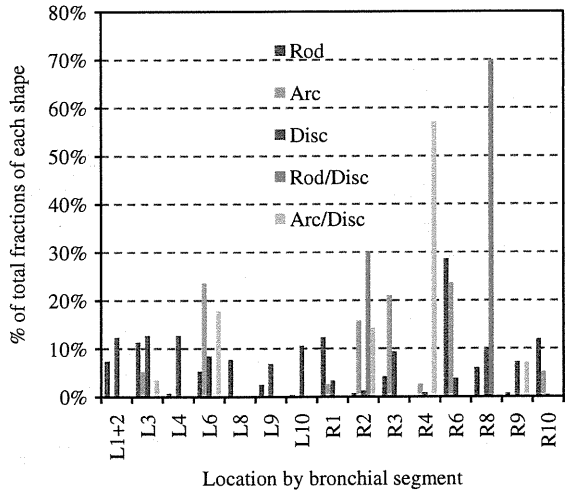

Figure 6. Distribution of motion space shapes normalized for each shape type.

3.3. Shape versus segment results

A comparison of the tumours' motion space shapes and the tumours' geometrical locations is shown in figures 6 and 7. Figure 6 shows that tumours exhibiting rod-like motion hulls were

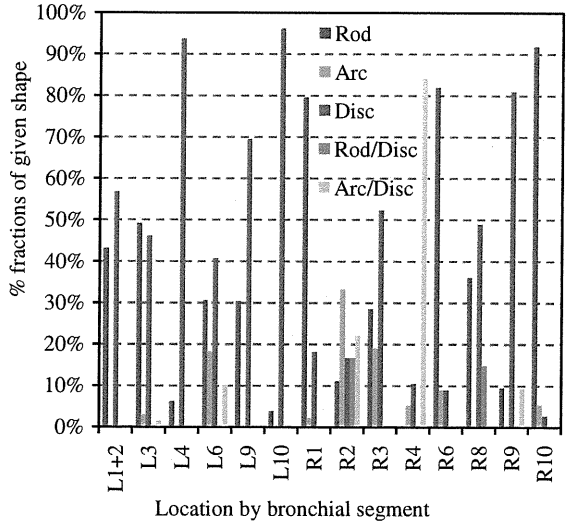

Figure 7. Distribution of hull shapes normalized by bronchial segments.

more likely to be located in the apex, with the exception being segment R^{10}. The hybrid shapes are almost exclusive to the right side of the lung, whereas the general shapes are distributed across both lungs.

For each bronchial segment, all treatment fractions for any tumour at that location have been considered in figure 7. The per cent of fractions of each convex hull shape are calculated, based on the five shapes described above. For example, 82% of fractions in segment R^6 had tumour motion that was enclosed by rod-like hulls, 9% by arc-shaped hulls and 9% by disc-shaped hulls. Results show that elliptical motion is more likely among tumours located in segments L^4, L^9, L^{10} and R^9. Arc paths are slightly more prevalent among tumours located in segments R^2 and R^3.

In a comparison of motion envelope volume and motion amplitude, where amplitude is defined as the maximum distance between any two points of the three breathing cycles for each treatment fraction, the correlation was found to be moderate ($R^2 = 0.602$), see figure 8 and table 2.

4. Discussion

The analysis revealed moderate correlation between tumour location and volume of motion. The comparison of convex hull shape and location was less conclusive. In general, motion increased with proximity to the diaphragm. Hysteresis was present in most locations, but slightly more prevalent in tumours closer to the diaphragm.

When deciding to remove an outlier data point, several considerations were made. The first regarded the data collection. The outlier data points were not identified as being corrupted by mechanical or electronic errors during collection nor were they considered to be noise. The points do, however, represent unlikely physical scenarios. One speculative explanation was coughing by the patient or some other reflex action. This was ruled out because, even with the abrupt change in path and increase in speed expected with a sudden reflex action, with a 30 Hz frame-rate, a trail of points would have been observed instead of the manifestly outlying

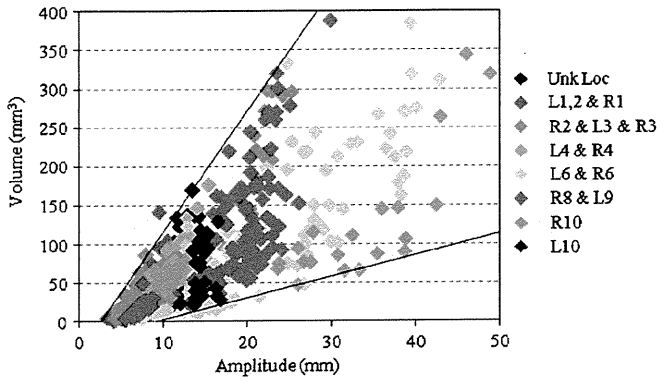

Figure 8. Amplitude versus volume. A comparison of motion amplitude and motion envelope volume. The locations correspond to figure 3(a).

points. A clinical consideration was dosimetry. One measure of the efficacy of a prediction model is its ability to deliver the prescribed dose to the target. The outliers identified in the data for a given treatment fraction substantially increased the size of the prediction space while only representing a fraction of a percentage of the data points. If a prediction model ignored the possibility of the types of outliers seen in the data, the dosimetric consequences would be partial treatment interruptions on the order of 0.1 s per treatment session. This would be negligible when compared to the dosimetric error that would result from a mis-prediction of a second or more.

Several improvements can be made to the volumetric analysis methods. The most useful improvement, as discussed above, would be a volumetric analysis by breathing state. This will involve the identification of breathing state based on the velocity vector of a given data point taken in conjunction with previous data points. Additionally, algorithms to calculate concave volumes would give more representative motion spaces for several of the previously identified shapes. The ability to give accurate concave volumes would also be necessary for the division of motion data into breathing states, especially if any curvature is to be captured. One potential way to do this involves a digitization of the motion data. This could be done by overlaying a 3D grid on the convex hull and including in the concave space any grid location that contains a data point. The ability to precisely calculate the motion space for a tumour at a given state of respiration will greatly enhance the ability to provide accurate predictions of tumour motion. Additional methods being explored include alpha-hulls (Edelsbrunner *et al* 1983) and convex encloses of CT style slices.

The finite-state model for patient respiration allows for four breathing states by the patient: inhaling (IN), exhaling (EX), end of exhalation (EOE) and irregular (IRR) (Wu *et al* 2004). For each state, there are allowable transitions to other states (i.e. IN to EX or IRR, EX to EOE or IRR, EOE to IN or IRR and IRR to any state). Depending on the duration, the patient has been in his or her current state, certain transitions are more likely, giving rise to the notion of a transition probability. The data presented in this article, when coupled with a finite-state model of respiration, may increase the predictive power of the model by identifying the motion space for a particular phase of respiration. Figure 9 illustrates the division of the motion from one treatment fraction into inhalation, exhalation and end of exhalation breathing states. In practice, as implemented in an online tumour tracking system with the predictive model of tumour motion behaviour, the tumour's path may be correlated to the patient's